Received: 7 August 2020 | Accepted: 30 November 2020

DOI: 10.1002/vzj2.20099

Vadose Zone Journal

SPECIAL SECTION: AGROGEOPHYSICS: GEOPHYSICS TO INVESTIGATE SOIL–PLANT–ATMOSPHERE INTERACTIONS & SUPPORT AGRICULTURAL MANAGEMENT

Toward high-resolution agronomic soil information and management zones delineated by ground-based electromagnetic induction and aerial drone data

Christian von Hebel[1,2] | **Sophie Reynaert**[3] | **Klaas Pauly**[4] | **Pieter Janssens**[3] | **Isabelle Piccard**[3] | **Jan Vanderborght**[1] | **Jan van der Kruk**[1] | **Harry Vereecken**[1] | **Sarah Garré**[2,5]

[1] Forschungszentrum Jülich, Institute of Bio- and Geosciences, Agrosphere (IBG-3), Jülich, Germany

[2] Agro-BioTech Gembloux, Univ. Liege, Gembloux, Belgium

[3] Soil Service Belgium (SSB), Gembloux, Belgium

[4] Vlaamse Instelling voor Technologisch Onderzoek (VITO), Gembloux, Belgium

[5] Research Institute for Agriculture, Fisheries, and Food (ILVO), Gembloux, Belgium

Correspondence
Christian von Hebel, Institute of Bio- and Geosciences, Agrosphere (IBG-3), Forschungszentrum Jülich, Germany.
Email: c.von.hebel@fz-juelich.de

Assigned to Associate Editor Benjamin Mary.

Funding information
H2020 Societal Challenges; Potential - Variable rate irrigation and nitrogen

Abstract

Detailed knowledge of the intra-field variability of soil properties and crop characteristics is indispensable for the establishment of sustainable precision agriculture. We present an approach that combines ground-based agrogeophysical soil and aerial crop data to delineate field-specific management zones that we interpret with soil attribute measurements of texture, bulk density, and soil moisture, as well as yield and nitrate residue in the soil after potato (*Solanum tuberosum* L.) cultivation. To delineate the management zones, we use aerial drone-based normalized difference vegetation index (NDVI), spatial electromagnetic induction (EMI) soil scanning, and the EMI–NDVI data combination as input in a machine learning clustering technique. We tested this approach in three successive years on six agricultural fields (two per year). The field-scale EMI data included spatial soil information of the upper 0–50 cm, to approximately match the soil depth sampled for attribute measurements. The NDVI measurements over the growing season provide information on crop development. The management zones delineated from EMI data outperformed the management zones derived from NDVI in terms of spatial coherence and showed differences in properties relevant for agricultural management: texture, soil moisture deficit, yield, and nitrate residue. The combined EMI–NDVI analysis provided no extra benefit. This underpins the importance of including spatially distributed soil information in crop data interpretation, while emphasizing that high-resolution soil information is essential for variable rate applications and agronomic modeling.

1 | INTRODUCTION

During the past centuries, agriculture succeeded in increasing yield production by enlarging field sizes, increasing

Abbreviations: CSM, classical soil map; EC_a, apparent electrical conductivity; EMI, electromagnetic induction; FCM, fuzzy *c*-means; NDVI, normalized difference vegetation index.

machinery, and using monoculture cropping systems and homogeneous agronomic management. This led to lower production costs, higher profits, vibrant agricultural supply sectors, and low food prices. On the other hand, this food production system invoked negative environmental impacts such as increased nitrogen and pesticide concentrations in ground- and surface waters, eutrophication, presence of chemical residues with potential health hazards in food, and difficulties for smaller family farmers to compete.

Reducing the agricultural impact on the environment and changing its paradigms is essential to solve these problems and move toward a sustainable agriculture. To turn the system and act sustainable, agriculture needs to scan the soil, measure the crops, and act on the intra-field variable soil conditions that drive the specific cropping areas. To support this shift and advocate sustainability, we need detailed knowledge of the soil, the crops, and the soil–crop interactions in the specific environmental and climatological conditions. At certain zones within the field, the soil holds vital plant resources where the crops need less or even no extra fertilizer, irrigation water, and/or agro-chemicals. Knowing the intra-field soil variability helps to save resources, since this information enables applying fertilizers, water, or pesticides only where needed (Cassman, 1999; De Benedetto et al., 2013).

Precision agriculture aims for site-specific and intra-field management systems based on observing and analyzing the differences in crop performance, often using remotely sensed satellite data (Mulla, 2013; Virnodkar, Pachghare, Patil, & Jha, 2020). The spatial resolution of satellite products has refined very much in recent years up to the meter scale as commercially offered, for example, by EOS (Earth Observation System, www.eos.com). Aerial drone-based measurements offer spatial crop data at centimeter-scale resolution (Mulla, 2013). This allows detailed investigations of the crop status. Understanding of agro-ecosystem functioning improves even further when spatially explicit soil information is available (Gonzalez-de-Santos et al., 2017; Maes & Steppe, 2019).

Based on this spatiotemporal information, agronomic models can produce high-resolution crop performance maps. Several platforms offering high-resolution crop data are available (e.g., SentinelHub, WatchITGrow, VITO). However, spatial soil data at similar resolution is less available. Even though the initial soil maps are typically being improved and/or updated (see Brevik et al., 2016), these remain coarse (around several hundreds of meters in resolution). To complement agronomic modeling results based on high-resolution aerial crop data, much denser soil data are required.

To identify and illuminate the within-field variability in agricultural soils, proximal sensing with noninvasive agrogeophysical methods such as electromagnetic induction (EMI) systems is a powerful tool (Corwin & Plant, 2005). Electromagnetic induction allows investigating the soil and the soil–plant interactions in the field with meter to submeter resolution (Doolittle & Brevik, 2014; von Hebel et al., 2018; Whalley et al., 2017). Agrogeophysics is also emerging in characterizing active root zones and/or root water uptake patterns of competing and mixed crops by using electrical methods (Garré et al., 2013; Mary et al., 2020; Weigand & Kemna, 2017).

Core Ideas

- Electromagnetic induction (EMI) enables delineation of high-resolution management zones.
- Management zone delineation using aerial crop data depends on acquisition time.
- Management zone delineation based on EMI data seems time independent.
- Important for variable rate applications, EMI-based delineated zones differ agronomically.

Due to their contactless operation, EMI systems allow measuring the apparent electrical conductivity (EC_a) distribution of large-scale agricultural fields in relatively short time (Corwin & Scudiero, 2019). The EC_a values reflect a range of physio-chemical soil attributes including soil texture, soil water, and soil salinity, as well as soil compaction and porosity, as shown in a wide range of studies (Abdu, Robinson, Seyfried, & Jones, 2008; Altdorff et al., 2017; Boaga, 2017; Calamita, Perrone, Brocca, Onorati, & Manfreda, 2015; Doolittle & Brevik, 2014; Heil & Schmidhalter, 2012; Huang, Koganti, Santos, & Triantafilis, 2017; Jadoon et al., 2015; Robinet et al., 2018; Saey et al., 2013; Zhu, Lin, & Doolittle, 2010). Therefore, analyzing the EMI data together with ground-truth soil samples collected in different zones in the field helps in identifying the field-specific soil attributes contributing to EC_a. In addition, the combination of ground-based EMI and aerial crop data can discover hidden soil–crop interactions (De Benedetto et al., 2013; von Hebel et al., 2018; Wang et al., 2019). This relatively new scientific direction emerged due to the increasing ability to remotely sense high-resolution crop information.

To delineate management zones for a given field, cluster analysis can use ground-based soil, remotely sensed satellite data, and/or combinations of the ground and aerial data (Grunwald, Vasques, & Rivero, 2015). For example, De Benedetto et al. (2013) combined EC_a and remotely sensed crop indices to identify different zones related to soil properties and crop response patterns in one field. Combining EMI and normalized difference vegetation index (NDVI) maps successfully delineated zones on three adjacent fields (Saifuzzaman et al., 2019), where the EC_a maps were consecutively measured within short time.

Traditionally, EC_a data are used for mapping and investigating soil properties and aerial data for investigating the crop performances and studies often concentrate and

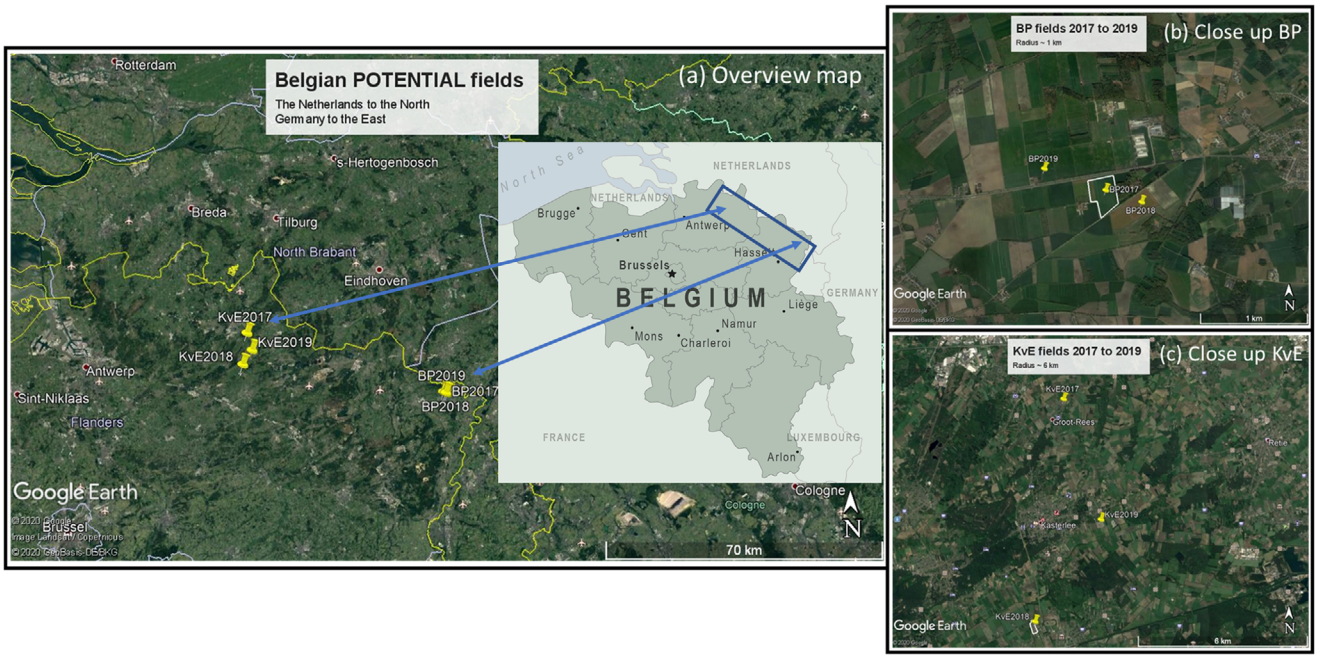

FIGURE 1 (a) Overview map of POTENTIAL fields. In the close ups for the Farmer 1 (BP) and Farmer 2 (KvE) farms in Panels b and c, respectively, the focus fields BP2017 and KvE2018 of this main article are framed in white

demonstrate data of one specific field. An analysis examining various fields and spanning over a longer period by performing a combined and separate analysis of ground-based geophysical soil and drone-based crop data, which are underpinned with ground-truth and in situ data, is still open.

This study aims to close this gap by using a series of six distinct potato (*Solanum tuberosum* L.) fields measured in 3 yr. We study the use of EMI, NDVI, and the combined EMI–NDVI datasets for delineating agronomic management zones. To interpret and quantify the differences between the resulting and field-specific management zones, we incorporate different levels of data diversity—namely, the temporal aerial drone-based NDVI images, the spatial EMI soil scanning maps, ground-truth point-scale soil samples, harvested yield information, and the nitrate residues in the soil. The presented study helps to vary rates of fertilization and irrigation while enabling to obtain high-resolution soil data, which is necessary for precision agriculture and agronomic modeling.

2 | MATERIALS AND METHODS

2.1 | Test site descriptions

2.1.1 | Basic description of nontreated and treated fields

This study was carried out in the framework of the POTENTIAL project that aimed at developing options for variable-rate irrigation and nitrogen fertilization in potato with collaborations between Germany, Belgium, Denmark, and the Netherlands. A background document with guidelines for variable rate applications are available in Janssens et al. (2020). For this study, six fields belonging to two farmers were scanned with EMI between 2017 and 2019. The fields were in the Campine region of northern Belgium (Figure 1). Three fields of Farmer 1 (BP) were within a radius of around 1 km, and three fields of Farmer 2 (KvE) were within a radius of 6 km, and the two farms were around 50 km apart.

Table 1 shows basic information of the agricultural management of the six fields investigated in the present study. At each of the six fields, the SSB (Soil Service of Belgium) selected up to 20 plots with either 10 or 15 m diameter and monitored two fields each year. The farmer managed the fields in a homogeneous way for potato cultivation, and SSB monitored soil and crop properties during the growing season. At one field per year, the plots were specifically treated (additional or fully reduced fertilization and irrigation amounts) and SSB monitored the effect of the treatments on the crop and soil variables. The locations of the plots were selected to compromise science and the farmer's needs. For the farmer, these were minimally disturbing the practice. For science, these were in most homogeneous regions to ensure comparability between the different treatments. The monitoring program at each plot included soil measurements (soil texture [sand, silt, and clay], bulk density, soil water content, water retention characteristics, and nitrogen content in soil), and in situ crop and yield observations such as tuber weight and amount of potatoes. The mean soil attributes as well as yield-related data are shown in Table 2. These indicate

TABLE 1 Basic description to the six fields used in the POTENTIAL project, including the UTM (Universal Transverse Mercator) coordinates, the soil texture class according to USDA, the cumulative precipitation, the irrigation, and fertilization amounts in the growing period, the potato variety, and the trial plot management

Descriptor	BP2017	KvE2018	BP2019	KvE2017	BP2018	KvE2019
x, *y* coordinates [UTM−31N]	688692, 5668948	637063, 5674498	687527, 5669151	637803, 5682472	689042, 5668941	639324, 5678271
Soil texture class	Sandy loam	Sand	Loamy sand	Loamy sand	Sandy loam	Sand
	Fertilization and irrigation management in the growing period (1 Apr.–31 Aug.)					
Precipitation, mm	203	187	204	225	156	306
Potato variety	Felsina	Zorba	Zorba	Zorba	Fontane	Felsina
N fertilization, kg ha^{-1}	200	169	191	181	221	200
Irrigation, mm	110	190	148	102	210	148
Trial plot management	Homogeneous	Homogeneous	Homogeneous	Treated	Treated	Treated

TABLE 2 Trial plot mean values and standard deviation of the soil attributes and yield information. Each field consisted of 8–20 trial plots. The diameters were either 10 or 15 m. The trial plots served for measuring the soil attributes and harvest information. At three fields, the farmer homogeneously managed the crops. At the other three fields, the N and irrigation amounts varied inside the trial plots to study management impacts on the crops and soil

Field name or attribute (0–30 cm)	BP2017	KvE2018	BP2019	KvE2017[a]	BP2018[a]	KvE2019[a]
Sand, %	71.9 ± 7.0	92.0 ± 1.1	77.0 ± 4.0	87.8 ± 1.3	65.0 ± 3.6	91.3 ± 1.6
Silt, %	23.0 ± 6	3.4 ± 0.4	18.0 ± 3.7	6.3 ± 1.4	26.9 ± 3.0	4.1 ± 1.0
Clay, %	5.1 ± 1.6	4.6 ± 0.9	5.0 ± 0.7	5.9 ± 0.8	8.1 ± 2.0	4.5 ± 1.1
BD, g cm^{-3}	1.43 ± 0.08	1.22 ± 0.08	1.51 ± 0.24	1.30 ± 0.06	1.51 ± 0.07	1.52 ± 0.05
SWC, cm^3 cm^{-3}	0.26 ± 0.03	0.27 ± 0.06	0.15 ± 0.01	0.18 ± 0.02	0.26 ± 0.03	0.16 ± 0.02
TAW, cm^3 cm^{-3}	0.32 ± 0.02	0.14 ± 0.02	0.17 ± 0.02	0.29 ± 0.08	0.23 ± 0.05	–
TWT, kg $m^{-š}$	5.8 ± 0.5	4.9 ± 0.4	6.0 ± 0.7	4.4 ± 0.8	5.1 ± 2.0	5.7 ± 1.0
TAT, no. $m^{-š}$	42 ± 3.4	27.7 ± 2.2	42.0 ± 3.8	52.9 ± 12.4	47.3 ± 6.4	10.8 ± 1.7

Note. BD, bulk density; SWC, volumetric soil water content; TAW, total available water = SWC (pF = 2) – SWC (pF = 4.2); TWT, total weight of tubers; TAT, total amount tubers.

[a]Fields with specifically treated plots.

easy-to-interpret information while being too coarse for variable-rate applications and precision agriculture. In addition to the in situ measurements, VITO (Vlaamse Instelling voor Technologisch Onderzoek) collected drone-based temporal crop data of NDVI during the growing season and the IBG-3 (Institute of Bio- and Geosciences, Agrosphere) performed EMI soil scanning before potato planting.

2.1.2 | Focus field descriptions

In the main article, we focus on the fields BP2017 and KvE2018 to keep the data visualization clear while the supplemental material contains additional results of all six fields. The soil distribution of the classical soil map (CSM) (van Ranst & Sys, 2000) essentially shows a loamy sand with two small edges of sand and sand loam in the northeastern and southwestern corners at the field BP2017 (Figure 2a), respectively. The soil at the field KvE2018 (Figure 2b) is sand with a negligible area of loamy sand in the northern part.

Tables 3 and 4 respectively list the soil attributes of the upper 30 cm measured at each trial plot for the fields BP2017 and KvE2018, as well as the exact date of the measurements. The soil sampling or start of the monitoring program was in late April (BP2017) and early May (KvE2018). Here, we add that a time gap was present between the large-scale EMI scanning (February–March) and the start of the trial plot monitoring program including soil sampling (April–May). For the soil textures, we assume these being constant over the time span (Robinson, Abdu, Lebron, & Jones, 2012). The soil water content and bulk density change with time. During both the EMI scanning (end of winter) and the soil sampling (early spring), the soil was probably at or near to field capacity with comparable soil water content. The bulk density was likely similar at the EMI scanning and program start because of flat soil (neither tilling nor potato ridge shaping).

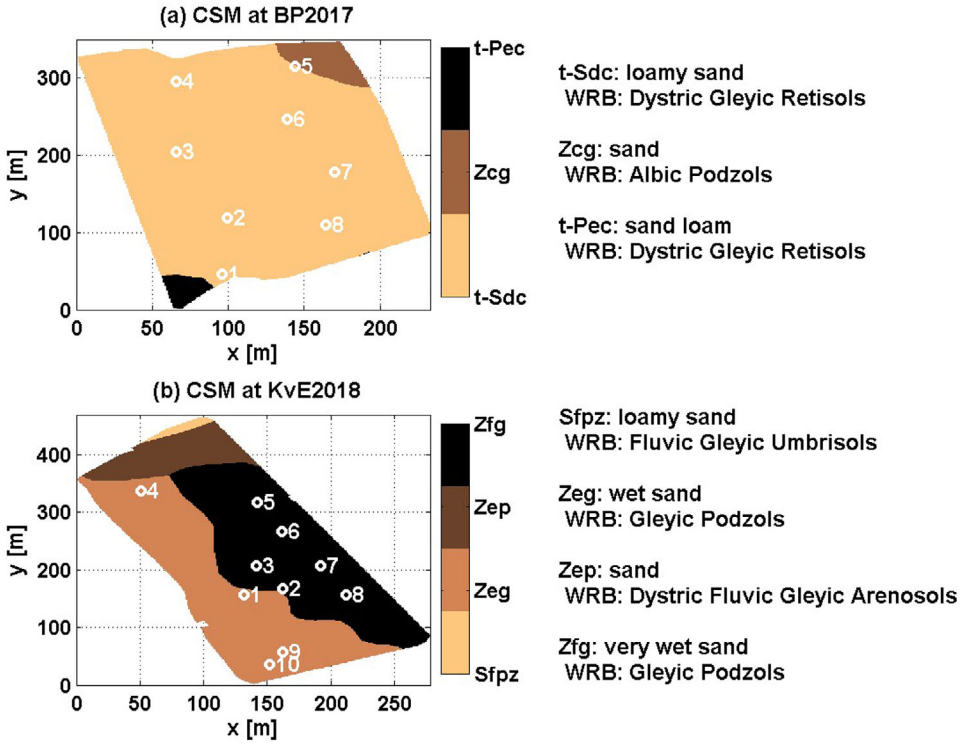

FIGURE 2 Classical soil map (CSM) of two of the six trial fields: (a) BP2017 and (b) KvE2018 with the respective 8 and 10 trial plot locations. The texture class and soil description are per the Soil Service of Belgium (SSB) and World Reference Base (WRB), respectively

2.2 | Surface based large-scale EMI data collection

2.2.1 | Principle of EMI and system descriptions

Electromagnetic induction systems generate magnetic fields. An alternating current energizes the transmitter at a fixed frequency to generate a primary magnetic field. This induces eddy currents in the soil, which in turn generates a secondary magnetic field (Ward & Hohmann, 1988). The receiver measures the superimposing primary and secondary magnetic field consisting of a real and an imaginary part (Keller & Frischknecht, 1966). The imaginary or quadrature part of the secondary to primary magnetic field is related an EC_a value (Beamish, 2011, Guillemoteau, Simon, Luck, & Tronicke, 2016, Hanssens, Delefortrie, Bobe, Hermans, & De Smedt, 2019, McNeill, 1980, von Hebel et al., 2019).

The secondary magnetic field strength is a function of the electrically acting soil attributes. Such attributes include soil texture (contents of sand, silt, and clay), soil water content, and bulk density beside soil salinity, soil pH, and soil organic

TABLE 3 BP2017 soil attributes of each trial plot sampled timely close to the electromagnetic induction (EMI) measurements

Trial plot no.	Sand	Silt	Clay	BD	SWC
	%			g cm^{-3}	cm^3 cm^{-3}
1	73.6	22.9	3.5	1.40	0.23
2	64.0	29.6	6.4	1.52	0.29
3	62.9	30.5	6.6	1.58	0.32
4	81.0	15.5	3.5	1.46	0.26
5	83.7	13.1	3.2	1.36	0.26
6	68.5	27.0	4.5	1.38	0.26
7	68.1	24.2	7.7	1.36	0.25
8	73.3	20.9	5.7	1.38	0.23

Note. Soil attributes measured at 21 Apr. 2017, EMI soil scan at 22 Feb. 2017. BD, bulk density; SWC, volumetric soil water content.

TABLE 4 KvE2018 soil attributes of each trial plot sampled timely close to the electromagnetic induction (EMI) measurements

Trial plot no.	Sand	Silt	Clay	BD	SWC
	%			g cm^{-3}	cm^3 cm^{-3}
1	90.5	3.6	5.9	1.14	0.33
2	93.0	2.8	4.2	1.32	0.22
3	91.0	3.4	5.6	1.21	0.23
4	90.9	4.1	5.0	1.04	0.27
5	90.6	3.5	5.9	1.30	0.37
6	93.3	3.7	3.0	1.21	0.22
7	93.6	3.0	3.4	1.22	0.20
8	93.1	2.7	4.2	1.29	0.35
9	92.2	3.4	4.4	1.21	0.22
10	92.2	3.4	4.4	1.23	0.26

Note. Soil attributes measured at 2 May 2018, EMI soil scan at 28 Mar. 2018. BD, bulk density; SWC, volumetric soil water content.

carbon (Altdorff et al., 2017; Brogi et al., 2019; Corwin & Lesch, 2005; Doolittle & Brevik, 2014; Huang, Scudiero, Choo, Corwin, & Triantafilis, 2016; Martini et al., 2016; Saey et al., 2013; Werban, Kuka, & Merbach, 2009). The main attributes can change with the history of the agricultural soil usage (Kaufmann et al., 2020) and generally change with the test site due to the unique soil compositions at each field. Soil sampling and analysis remain necessary to interpret the field specific soil attributes based on EC_a.

In this study, we used the CMD-MiniExplorer (GF Instruments, 2011) manufactured by GF-Instruments, which operates at 30 kHz to record the large-scale EC_a distribution using vertical coplanar coils with 71-cm distance between transmitter and receiver. This coil configuration measures a depth range of approximately 0–50 cm and shows the largest sensitivity at the surface falling rapidly with depth. Since the upper soil mostly contribute to the signal, the EC_a measured with this coil configuration is representative for a soil depth that corresponds to the soil used for attribute analysis (0-to-30-cm depth), as well as the approximate soil depth used for potato ridge shaping.

At each field, we inserted the EMI systems into plastic sleds. Before the large-scale soil scanning, the EMI systems warmed up for ~30 min. In this time, the differential global positioning systems (RTX center point DGPS system of Trimble) converged to centimeter accuracy. During the measurements, a quad-bike dragged the sleds along parallel tracks with spatial distances of 2 m to 3 m. The inline sampling was ~ 30 to 40 cm, resulting in a driving speed from 5 to 8 km h^{-1} and a sampling rate of 5 Hz. Depending on the field size, the EMI scanning recorded 25,000 to 50,000 EC_a values as illustrated in Figure 3a and 3c, respectively, shown for the BP2017 and KvE2018 fields, where the black border indicates the drone data acquisition area. The EC_a maps of all six fields are shown in the supplemental material.

2.2.2 | EMI data processing

The EMI system is factory calibrated for the supplied crutch handle, as well as stable against moderate temperature variations (GF Instruments, 2011). Since we use our sled setup and aim at patterns for management zone delineation, the parameters found by von Hebel et al. (2019) turn the sled-based EC_a to handle-based values. When the data need to be quantitative for reliable inversion results to compute a subsurface model with layer/horizon depths, this can be obtained when calibrating the EC_a against independent geoelectrical data (Binley et al., 2015; Cavalcante Fraga, Schamper, Noël, Guérin, & Rejiba, 2019; Heil & Schmidhalter, 2019; Lavoué et al., 2010; Mester, van der Kruk, Zimmermann, & Vereecken, 2011; von Hebel et al., 2014; Whalley et al., 2017) or when using an EMI system-based numerical calibration procedure (Hunkeler, Hendricks, Hoppmann, Paul, & Gerdes, 2015; Minsley, Kass, Hodges, & Smith, 2014; Tan et al., 2018).

To tackle the outliers, the histogram filter method (von Hebel et al., 2014) sieved the EC_a values. This filter method performed successfully in a range of studies (Brogi et al., 2019; Kaufmann et al., 2020; Wang et al., 2019) and uses the following steps. The first filter removes too large and too small values defined by the user. A second filter uses histogram bins and remove those carrying less data than a threshold (here set to 0.1% at all fields). In a third step, the filter identifies and discards EC_a values that deviate from adjacent positions. Here, 2 mS m^{-1} difference was set for all fields as threshold between the 30- to 40-cm distant measurements. This strategy kept ~95% of all EC_a values at each of the six fields. The nearest neighbor interpolation TriScatteredInterp of Matlab (The Mathworks) finally obtained regular EC_a maps with 1-m grid node distance. Figures 3b and 3d for the fields BP2017 and KvE2019, respectively, show that due to the dense measurement tracks, the small-scale patterns present in the field

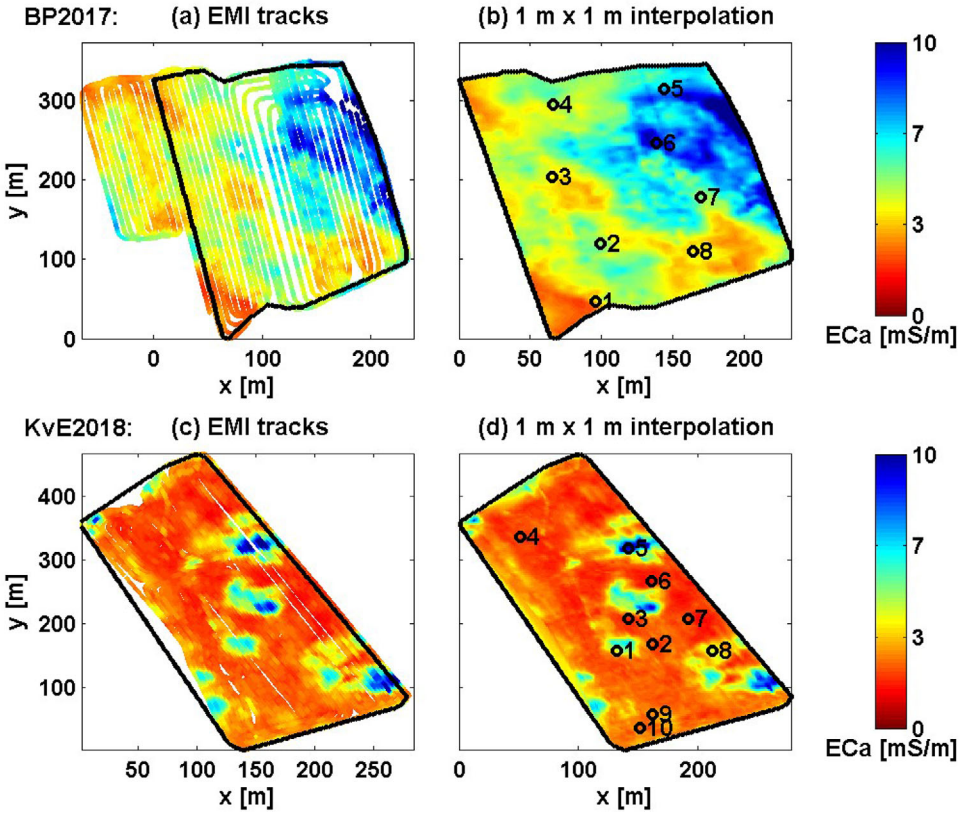

FIGURE 3 Processing of the apparent electrical conductivity (EC_a) data. The upper and lower rows correspond to the BP2017 and KvE2018 fields, respectively. Panels a and c show the data along the measurement tracks, and Panels b and d show the data interpolated to the 1-m × 1-m grid and the locations of the trial plots. EMI stands for electromagnetic induction

were well resolved in the 1-m × 1-m interpolated maps with no exaggeration, which often appear when using wide track distances.

2.3 | Aerial NDVI data

2.3.1 | Multispectral sensor characteristics and image acquisition

We used a Parrot Sequoia camera (Parrot Drone SAS) mounted on the senseFly eBee drone (senseFly, Cheseaux-Lausanne, a Parrot Group company) to collect high-resolution (8-cm pixels) temporal NDVI data during the growing season at three to eight flights depending on the field and year (compare NDVI temporal images in the supplemental material). To obtain the images, we performed the following acquisition, calibration, and processing steps.

The commercially available eBee drone is a remotely piloted aircraft system equipped with fixed wings. We flew the drone at a nominal flight height of 85 m above ground level, which ensured collecting high-resolution images by the multispectral camera. This camera consists of four synchronized single-band cameras. Each camera uses a 1.2-megapixel sensor with a 3.75-µm pixel pitch and a 4-mm lens, while using different interference filter. The filters enable simultaneous measurements in four spectral regions: one in the green (550 ± 20 nm), one in the red (660 ± 20 nm), one in the red-edge (720 ± 10 nm), and one in the near-infrared (790 ± 20 nm) band. This generated four 16-bit tiff images at each acquisition point (each with a slight offset in the field of view).

A commercial lightweight GPS– Inertial Measurement Unit (IMU) system attached to the drone tracked the acquisition points, and an upward-looking irradiance sensor array with a diffuser plate on top delivered the specific irradiance values using the same interference filter as the multispectral camera. At each field, we installed five artificial control point markers on the ground to improve the geometric camera calibration and to ensure accurate co-registration across the temporal datasets. The control points were commercially available 1-m^2 36% reflectance gray tarp markers with factory-supplied reflectance spectrum, which we used for independent spectral and radiometric verification. The position of these ground control points were accurately located using a differential GPS, which additionally corrected the drone GPS–IMU coordinates (positional and rotational accuracy in the meter and degree range, respectively) to centimeter accuracy.

2.3.2 | Image processing

For the image processing, the Agisoft Metashape 1.5.x software performed a structure from motion photogrammetry workflow. This workflow consists of tie-point extraction and matching (alignment) and geometric camera calibration, as well as refinement of the georeferencing (optimization). Additional steps were reflectance calibration, dense point cloud generation, and their classification into ground, aboveground, and noise classes. The generation of a raster digital surface model and a digital terrain model finally results in the reflectance orthomosaic.

2.3.3 | Radiometric and spectral calibration

The Parrot Sequoia delivery includes a 10-cm × 10-cm gray reflectance calibration panel (outfitted with a bubble level) with factory-supplied reflectance values for the four multispectral bands. This panel served for camera calibration before and after each flight. For this, we held the airplane over the panel and acquired three four-band images, while the centered panel filled a significant portion of the camera view. The sun was behind the drone, and neither shadows nor reflections were on the panel or on the irradiance sensor.

In Agisoft Metashape, a reflectance calibration module allows digitizing regions of interest on each spectral band image for the images containing the panel. Then, the module executes a digital number-to-reflectance calibration using an empirical line method and transfers the results to all images considering the irradiance sensor values.

2.3.4 | Vegetation index extraction

Each reflectance orthomosaic was transferred to NDVI maps using the available reflectance bands, where R_{NIR} and R_{Red} are the reflections in the near infrared (790 nm) and red (660 nm) spectra, respectively:

$$\mathrm{NDVI} = \frac{R_{NIR} - R_{RED}}{R_{NIR} + R_{RED}} = \frac{R_{790} - R_{660}}{R_{790} + R_{660}} \quad (1)$$

Note that we masked out the pixels containing bare soil and only keep the vegetation information.

2.3.5 | Down sampling and rotation of high-resolution NDVI data to farming-grid

The orhtomosaic NDVI maps with 8-cm pixel size shown in Figures 4a and 4c for the BP2017 and KvE2018 fields, respectively, allow identifying details on single crops, which can be used to identify differences in the crop status (Janssens et al., 2020). These were scaled to the 1-m × 1-m EMI grid using the Matlab function interp2 (see Figures 4b and 4d). Since information on a 1-m × 1-m grid is less suitable for common land machinery, we implemented a semiautomatic upscaling and rotation approach to delineate manageable zones. To identify the rotation angle, we observed the crop rows as indicated by the lines in Figures 4b and 4d for the BP2017 and KvE2018 fields, respectively, and tested different angles to find the best match. The correct angle rotated the grid, and the interp2 function of Matlab scaled up the maps. The grid size here was 10 m in the x direction and 5 m in the y direction, which compromises resolution on the one hand and the dimension for land machinery on the other hand. In principle, any size is feasible in our semiautomatic upscaling and rotation approach, which may be useful for optimizing infield route planning to reduce soil compaction, labor costs, fuel consumption, and field trafficking intensity (Edwards et al., 2017).

2.4 | Machine learning for management zone delineation

The machine learning algorithm used here is the fuzzy c-means (FCM) clustering method introduced by Bezdek (1981). The FCM is an unsupervised continuous classification procedure (McBratney & de Gruijter, 1992), where the clusters contain similar data that are as dissimilar to the other clusters. The FCM algorithm is a soft clustering technique. Each data point belongs to a certain cluster only to some degree, which is expressed by a membership value (Schröter et al., 2017). A higher value for the data point indicates a larger certainty in the cluster assignment (Martinez, Vanderlinden, Ordóñez, & Muriel, 2009; Stetco, Zeng, & Keane, 2015). Since our approach combines data of different bio-physio-chemical nature and their temporally changing dependencies, the FCM algorithm is more suitable to identify the zones of different soil and crop interactions potentially present in the fields as compared with other hard clustering methods such as k means that use binary decision to assign a datum to a cluster (Panda, Sahu, Jena, & Chattopadhyay, 2012). The FCM is also a standard tool in many scientific software packages (Castrignanò et al., 2018; Gili, Álvarez, Bagnato, & Noellemeyer, 2017; Nawar, Corstanje, Halcro, Mulla, & Mouazen, 2017) and is used relatively fast as compared with advanced computational and statistical methods that can find hidden links in soil and crop interaction (Kamilaris & Prenafeta-Boldú, 2018; Wang et al., 2019).

Before the clustering, the EMI and NDVI data were z transformed (data minus mean and divided by standard deviation). For the spatiotemporal analysis, we used the FCM implementation of Matlab. An important issue in the clustering

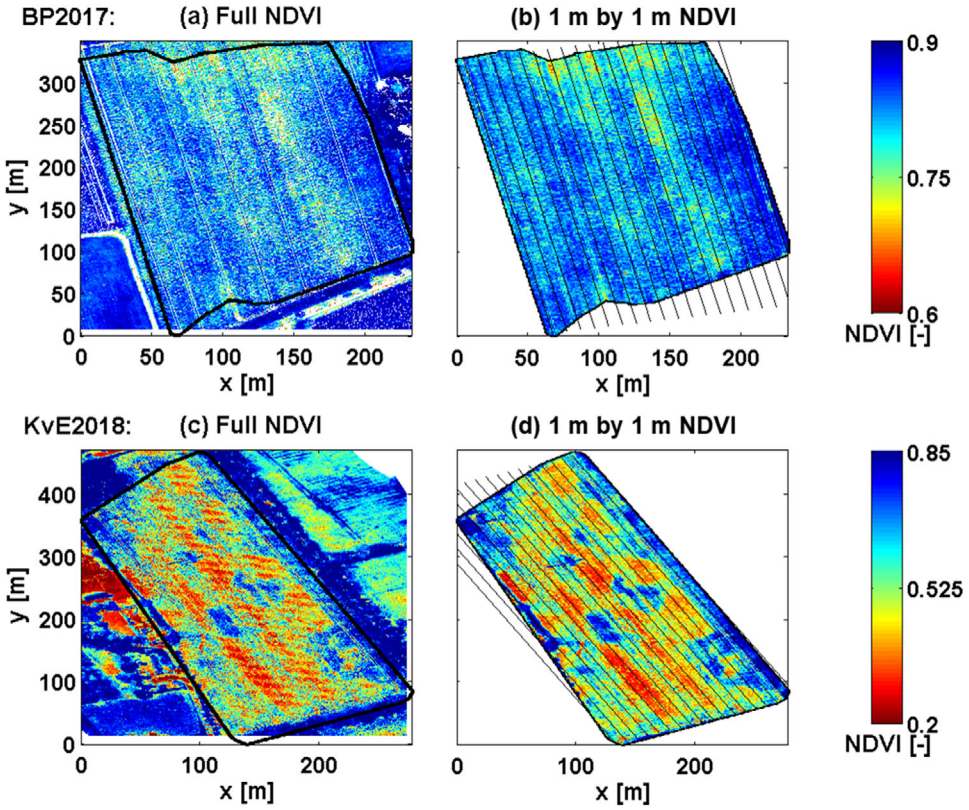

FIGURE 4 Normalized difference vegetation (NDVI) data. The upper and lower rows correspond to the BP2017 and KvE2018 fields, respectively. Panels a and c show the drone based full resolution (8 × 8 cm) data measured by Vlaamse Instelling voor Technologisch Onderzoek (VITO) using the multispectral camera. These data were scaled to a resolution of 1× 1 m as shown in Panels b and d that also show the 10-m separated lines parallel to the potato crop rows

procedure is to choose the number of clusters. Here, we tested two to five clusters assuming heterogeneity in the field and present the outcome of the algorithm (i.e., we keep every pixel of the clustering results to show the strength of the approach). To objectively decide the appropriate number of clusters, the silhouette method (Rousseeuw, 1987) allows the user to compare the quality of the clusters. Furthermore, this method is especially useful for identifying compact and widely separated clusters (Kaufman & Rousseeuw, 1990) as we seek in our management zone delineation for agricultural purposes.

The silhouette values measure how similar a data point is to its own cluster (cohesion) compared with other clusters (separation). This cohesion-separation value therefore indicates how well the data points have been classified and range from −1 to 1. The positive one means that the data point fully belongs to the assigned cluster. A silhouette of zero indicates that a data point could equally belong to other clusters. A value of 0.5 indicates a weak cohesion separation. A negative value indicates that the data point has been misclassified. The Matlab internal silhouette function evaluated the test of two to five clusters per field, and the mean silhouette value eventually indicated the appropriate number of clusters.

Once the management zones were delineated, the soil attributes corresponding to the zones were tested against the null hypothesis that the zones are similar given a significance level. The ttest2 function of Matlab was used that performs a two-sample t test testing whether the soil attributes in the different zones come from distributions with equal means at the significance level. The result $H = 0$ indicates that the null hypothesis ("means are equal") cannot be rejected. When $H = 1$, this indicates that the null hypothesis can be rejected and the differences between the zones are statistically significant.

3 | RESULTS AND DISCUSSION

3.1 | Farming-grid CSM, EMI, and NDVI maps

Figure 5 shows the data on the rotated and scaled farming grid. The EMI data of the field BP2017 (Figure 5b) roughly shows a southwest- to northeast-directed gradient. The EC_a was around 1 mS m^{-1} in the southwest and around 10 mS m^{-1} in the northeast. The field KvE2018 (Figure 5f)

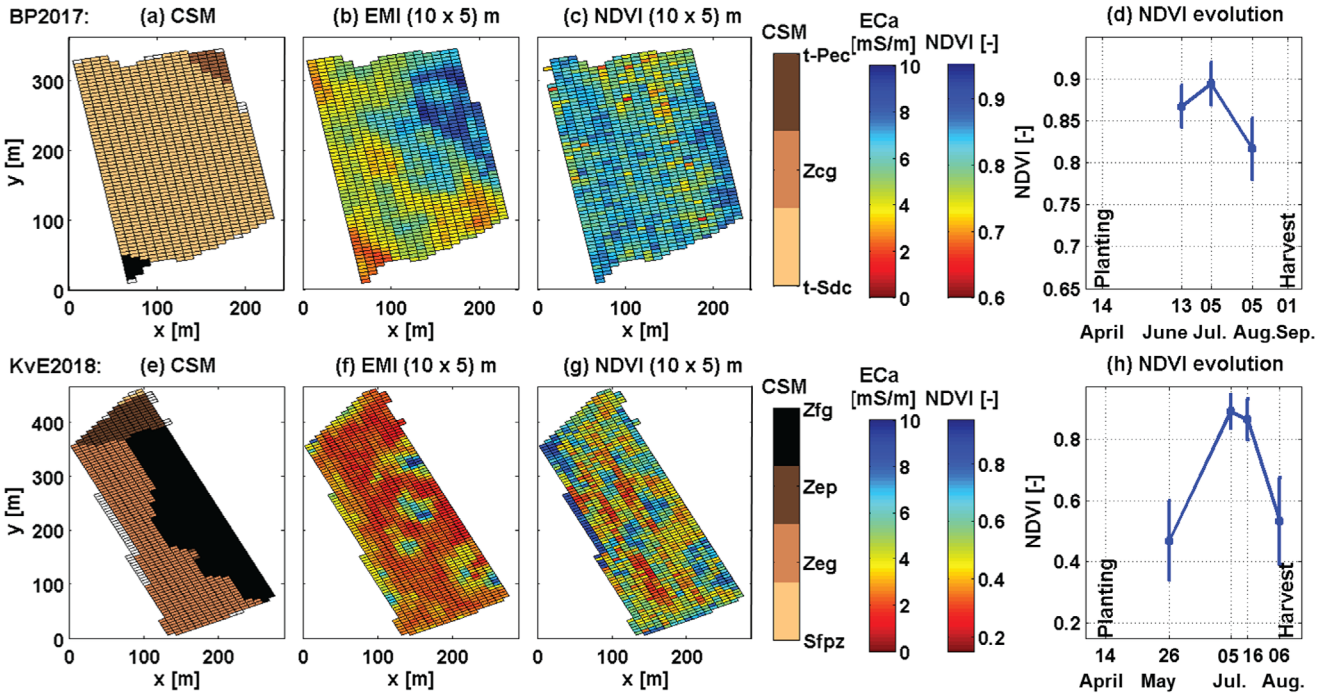

FIGURE 5 Large-scale maps at the farm-use grid: in the top row, field BP2017, and in the lower row, field KvE2018 fields. Panels a and e show the classical soil map (CSM) data, Panels b and f show the electromagnetic induction (EMI), Panels c and g show the normalized difference vegetation (NDVI) data, and Panels d and f show the NDVI evolution over the drone flights, as well as the potato planting and harvest dates

contained relatively small distinct areas of increased EC_a values up to 10 mS m^{-1}. These patches were distributed in a generally low (<3 mS m^{-1}) electrically conductive area.

The NDVI maps of all dates for each of the six fields are presented in the supplemental material, whereas Figures 5c and 5g show the NDVI maps of the fields BP2017 and KvE2018 measured toward the end of the growing season. At this stage, we expected to see differently senescing crops in different zones in the fields. For the field BP2017, planting was on 14 Apr. 2017, harvesting was on 1 Sept. 2017, and the last drone flight imaged in Figure 5c was on 5 Aug. 2017. As shown in Figure 5d, the mean NDVI during the last flight was lower than in July, which indicates that the potatoes started entering the senescence phase. However, the values were around 0.8 (Figure 5d), indicating well-performing crops and dense green vegetation (Rascher et al., 2015; von Hebel et al., 2018). As a result, the clear soil patterns scanned by EMI (Figure 5b) were not visible in the NDVI data. Note that Sentinel-2 satellite images acquired few days before harvest and close to senescence (Janssens et al., 2020) showed spatially different performing crops, which potentially allow investigation of soil–crop interaction in that field.

The NDVI data measured few days before the harvest (see Figures 5g and 5h) showed NDVI values around 0.3 in the largest part of the field indicating senescent potatoes and/or stressed crops. At the few small distinct patches, the crops were still performing well with NDVI values of around 0.85. Here, the crop data reflect the highly heterogeneous soil, and knowing the intra-field soil variability therefore helps explaining patterns in crop performances, which can consequently help guiding systems for variable rate applications.

3.2 | Agronomic properties in management zones

3.2.1 | Delineating management zones

We use the z-transformed ground-based EMI and aerial NDVI maps as single and combined datasets in FCM clustering to delineate management zones. Since crops likely show distinctive spatial patterns toward the end of the growing season, especially in dry periods, the NDVI map of the last date of data acquisition was used in the FCM algorithm. The EMI maps reflect the soil and were measured before potato planting and ridge shaping such that their combination with the NDVI data may indicate spatiotemporal soil and crop interaction.

In Figure 6, two clusters were used to delineate management zones using the single and combined datasets of the focus fields BP2017 and KvE2018. The mean silhouette values [μ(sil.)] served as goodness indicator of the cohesion-separation classification. At the field BP2017 shown in Figure 6a, the NDVI-based clustering results were highly scattered due to still green vegetation present during the drone flights. At that phase of the growing stage, the homogeneous

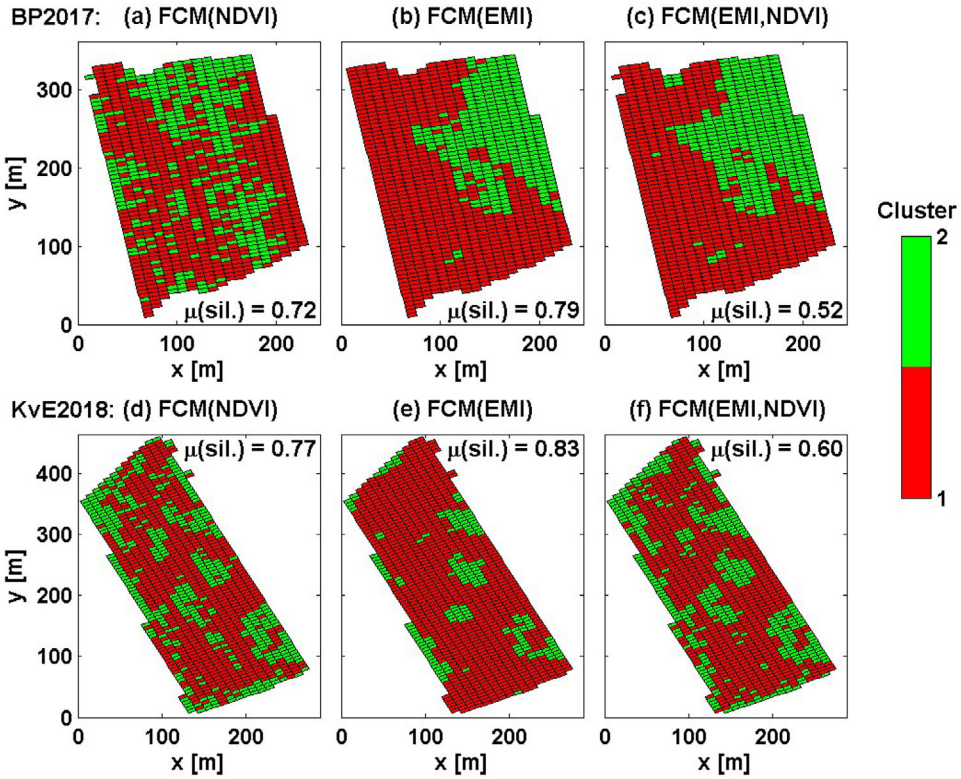

FIGURE 6 Fuzzy *c*-means (FCM) clustering results for two clusters together with the mean silhouette values, [μ(sil.)]. The top row shows the field BP2017 and the lower row shows the field KvE2018. In Panels a and d, the FCM used the normalized difference vegetation (NDVI) data only. In Panels b and e, the FCM algorithm clustered the electromagnetic induction (EMI) data. In Panels c and f, the FCM used the combined EMI and NDVI data

management seem to mask soil heterogeneity. At the field KvE2018, the NDVI data were obtained a few days before the harvest (compare Figure 5g here and the time series in the supplemental material), and the clustering obtained relatively clear delineated zones. At this stage, strong crop growth patterns were visible and closely related to soil heterogeneity (compare Figures 5f and 5g).

When using the EMI data of the field BP2017 (Figure 6b), two zones with northwestern–southeastern border were clearly delineated. At the field KvE2018 (Figure 6e), the patches of increased crop performance were distinctly visible. The μ(sil.) was around 0.8 for both fields indicating a good cohesion-separation of the clusters. Adding the NDVI data to the analysis as shown in Figures 6c and 6f for the BP2017 and KvE2018 fields, respectively, the clustering results changed and the μ(sil.) decreased.

The clustering using the NDVI and the EMI data of the field BP2019 obtained similar results: highly scattered vs. clearly delineated zones for the NDVI and EMI-based clustering, respectively. The combined EMI–NDVI data negligibly changed the delineated zones as compared with the clusters based on the EMI data. In order to understand the clustering results, Figure 7 shows the *z*-transformed EMI and NDVI data distributions and the data according to the clusters using the combined analysis. The histograms and scatter plots indicate that the data distributions of EC_a and NDVI over the field are unimodal and that, except for the KvE2018 field, there is no correlation between these two variables. The skewness of the distribution makes that the pixels are not equally distributed between the two clusters so that the cluster that represents the extreme values in the tail of the distribution covers a smaller area of the field. The clustering of the combined EC_a and NDVI dataset mainly clustered the dataset based on the EC_a values. We attribute this to differences in the shape of the EC_a and NDVI distributions. The clustering algorithm will split the dataset so that data points with the largest absolute *z* values are separated. When the two variables are not correlated and both have a unimodal distribution, this means that the algorithm will split the dataset according to the variable that shows the most and largest absolute z values (EC_a data) and will be less influenced by the other variable (NDVI data). The delineation of management zones using drone NDVI data only depends on the timing of the flights. This may improve when adding satellite data that, depending on the scope, may have too coarse resolution. On the other hand, we see the strong impact of the time-invariant soil patterns reflected by EC_a on the clustering. The spatial soil textural distribution that has a strong impact on EC_a can be considered stable such that the

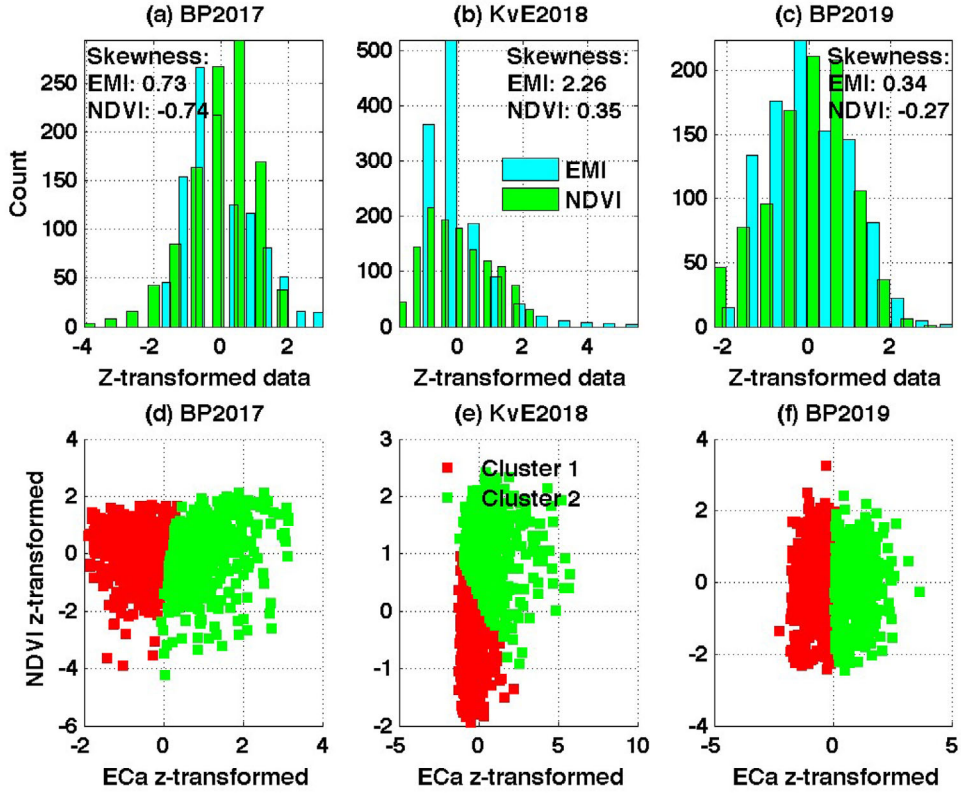

FIGURE 7 Distribution of the normalized electromagnetic induction (EMI) and normalized difference vegetation (NDVI) data in the upper row, as well as the cluster data in the lower row for the fields (a, d) BP2017, (b, e) KvE2018, and (c, f) BP2019. EC_a is the apparent electrical conductivity

shape of the spatial patterns will be the same for a measurement at another time given the same setup and data processing. This indicates that EMI data can delineate management zones independent of the timing.

We tested two to five clusters for management zone delineation based on the EMI data for all six fields, and Table 5 lists the corresponding mean silhouette values. For the focus fields BP2017 and KvE2018, the decreasing μ(sil.) with increasing number of clusters shows that two zones appropriately classify the field. At the third homogeneously managed field BP2019, two zones [μ(sil.) = 0.75] or three zones [μ(sil.) = 0.74] seem appropriate to delineate the field. At the three fields containing the treated trial plots (KvE2017, BP2018, and KvE2019), the optimal number of clusters was four, four, and two.

Summarizing two management zones was optimal for the investigated fields except of the fields KvE2017 and BP2018. At these fields, it was more appropriate to delineate four clusters. However, the differences in the μ(sil.) for four and two clusters were relatively small (see Table 5). Next, Table 6 compares the differences between the mean apparent electrical conductivity and the corresponding portion of the area for the two fields KvE2017 and BP2018, where four clusters obtained the largest silhouette values. Comparing this optimal

TABLE 5 Mean silhouette [μ(sil.)] values of the two- to five-cluster test for the electromagnetic induction (EMI) clustering at all six fields

Field	2-cluster μ(sil.)	3-cluster μ(sil.)	4-cluster μ(sil.)	5-cluster μ(sil.)
BP2017	0.79	0.68	0.69	0.68
KvE2018	0.83	0.77	0.72	0.70
BP2019	0.75	0.74	0.69	0.71
KvE2017[a]	0.72	0.72	0.74	0.72
BP2018[a]	0.64	0.67	0.70	0.69
KvE2019[a]	0.76	0.73	0.72	0.70

[a]Fields with treated trial plots.

TABLE 6 Mean apparent electrical conductivity (EC_a) and percentage of area for two clusters compared with the cluster results with the largest mean silhouette value [μ(sil.)]

	Cluster 1		Cluster 2		Cluster 3			Cluster 4
No. cluster	$\mu(EC_a)$	Area	$\mu(EC_a)$	Area	$\mu(EC_a)$	Area	$\mu(EC_a)$	Area
	mS m^{-1}	%	mS m^{-1}	%	mS m^{-1}	%	mS m^{-1}	%
KvE2017								
2	4.0	68	5.4	32	–	–	–	–
4[a]	3.7	44	4.6	36	5.6	18	7.7	2
BP2018								
2	6.1	51	9.1	49	–	–	–	–
4[a]	6.6	41	8.5	40	11.2	10	3.5	9

[a]Optimal clustering result (see Table 5).

number of clusters with the results of two management zones, increasing the number of clusters decreases the portion of the area. This is expected, while the differences in the mean EC_a were small. The additional clusters mainly incised the smaller management zone. To avoid this, setting a minimum areal size for the clusters or a post-classification removing small clusters can be implemented. This essentially reduces the number of zones. Here, we set two zones as appropriate, which seem sizably well for variable rate management.

3.2.2 | Soil attributes and yield information in the delineated management zones

Figure 8 shows the final EMI-based management zones with no simplification such as redrawing of small patches after the clustering. In order to check and verify the differences in the delineated zones, we used the information measured in the trial plots of the homogeneously managed fields. At the three fields BP2017, KvE2018, and BP2019, those plots that

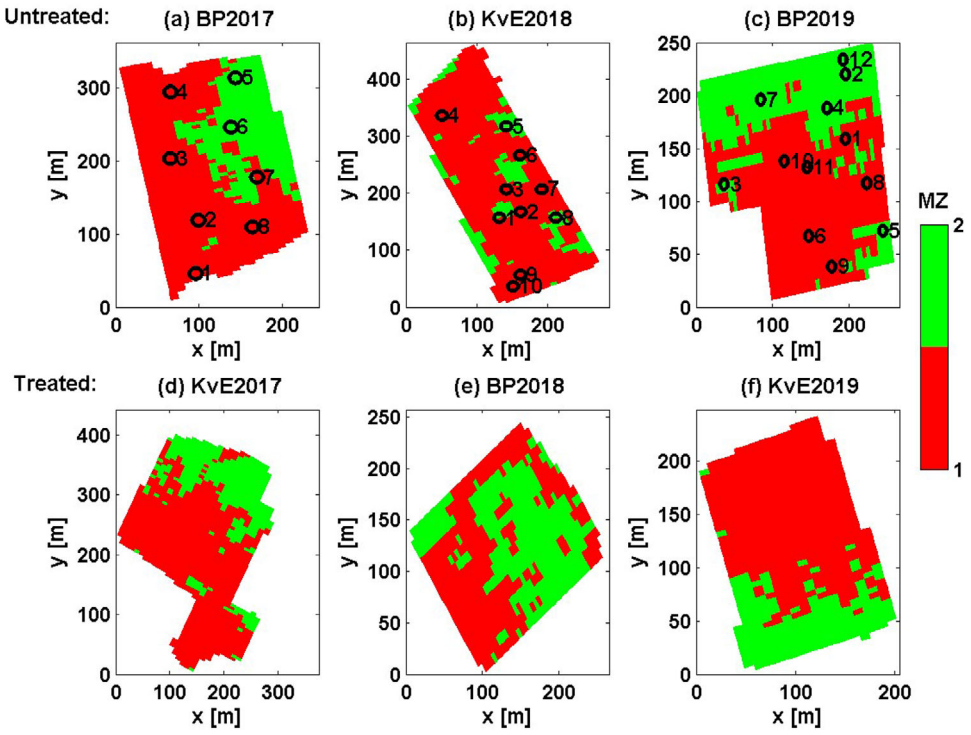

FIGURE 8 Management zones (MZs) for the six fields based on the electromagnetic induction (EMI) data. Panels a–c show the homogeneously managed fields with the positions of the trial plots. Here, we use the soil attribute information measured in these plots. For completeness, Panels d–e show the finally delineated zones of the specifically treated fields used for monitoring the effect of fertilization and irrigation on the potatoes

TABLE 7 Management zone (MZ) information using following data of the trial plots

Trait	BP2017		KvE2018		BP2019	
	MZ 1	MZ 2	MZ 1	MZ 2	MZ 1	MZ 2
Trial plots						
EMI-based	2, 3, 4, 8	5, 6	2, 3, 4, 6, 9, 10	5, 8	6, 9, 10, 11	2, 4, 5, 7, 12
NDVI-based	2, 3	4, 7	2, 3, 6, 9	5, 8	2, 4, 5, 8	3, 11
Texture class[a]						
EMI-based	sL	lS	S	S	sL to lS	sL to lS
NDVI-based	sL	sL	S	S	LS to sL	lS
Clay, %						
EMI-based	4.3 ± 1.4	3.9 ± 0.9	4.4 ± 0.9	5.0 ± 1.2	5.0 ± 0.5	5.3 ± 0.7
NDVI-based	6.5 ± 0.2	5.6 ± 3.0	4.3 ± 1.1	5.0 ± 1.2	4.8 ± 1.0	5.1 ± 0.7
Silt, %						
EMI-based	24.1 ± 7.2	20.0 ± 9.8	3.5 ± 0.4	3.1 ± 0.6	18.2 ± 3.7	19.1 ± 4.8
NDVI-based	30.0 ± 0.7	24.1 ± 6.1	3.3 ± 0.3	3.1 ± 0.6	19.4 ± 5.4	18.3 ± 0.8
Sand, %						
EMI-based	70.3 ± 8.5	76.1 ± 10.7	92.1 ± 1.0	91.9 ± 1.8	76.8 ± 3.9	75.6 ± 4.7
NDVI-based	63.5 ± 0.9	70.3 ± 9.1	92.4 ± 1.0	91.9 ± 1.8	75.7 ± 5.7	76.6 ± 1.5
BD, g cm^{-3}						
EMI-based	1.48 ± 0.09	1.37 ± 0.01	1.20 ± 0.09	1.30 ± 0.01	1.57 ± 0.06	1.43 ± 0.39
NDVI-based	1.55 ± 0.04	1.41± 0.07	1.2 ± 0.05	1.30 ± 0.01	1.0 ± 0	–
EC_a, mS m^{-1}						
EMI-based	4.2[b] ± 0.6	7.9[b] ± 1.3	2.1[b] ± 0.4	6.3[b] ± 3.5	3.3[b] ± 0.5	5.7[b] ± 0.8
NDVI-based	4.3 ± 0.7	4.9 ± 0.2	2.1[b] ± 0.5	6.3[b] ± 3.5	4.7 ± 1.0	4.3 ± 1.0
NDVI						
EMI-based	0.82[b] ± 0.02	0.77[b] ± 0.02	0.43[b] ± 0.06	0.61[b] ± 0.01	0.36 ± 0.03	0.37 ± 0.02
NDVI-based	0.83 ± 0.01	0.80 ± 0.02	0.40[b] ± 0.03	0.61[b] ± 0.01	0.38[b] ± 0.01	0.36[b] ± 0.002
SMD, cm^3 cm^{-3}						
EMI-based	0.06 ± 0.005	0.04 ± 0.003	0.01[b] ± 0.006	−0.01[b] ± 0.001	0.03 ± 0.02	0.02 ± 0.006
NDVI-based	0.06 ± 0.003	0.05 ± 0.01	−0.01[b] ± 0.004	−0.01[b] ±0.001	0.02 ± 0	–
Yield, kg ha^{-1}						
EMI-based	59,970 ± 5,800	54,440 ± 4,860	47,640 ± 3,090	50,740 ± 6,130	58,890 ± 12,660	60,260 ± 4,780
NDVI-based	63,010 ± 410	59,300 ± 4,630	47,750 ± 2,500	50,740 ± 6,130	59,370 ± 5,000	58,900 ± 624
Potato, no. ha^{-1}						
EMI-based	444,440 ± 22,460	427,220 ± 25,930	269,810 ± 27,010	277,780 ± 9,430	457,500[b] ± 40,160	397,780[b] ± 30,460
NDVI-based	435,560 ± 22,000	417,780 ± 77,000	282,500 ± 23,300	277,780 ± 9,430	397,220 ± 33,610	401,670 ± 5,500
NO_3 res., kg ha^{-1}						
EMI-based	24 ± 10	33 ± 6	133[b] ± 33	73[b] ± 19	79[b] ± 18	107[b] ± 25
NDVI-based	19 ± 2	21 ± 0	133[b] ± 25	73[b] ± 19	116 ± 38	81 ± 16

Note. Soil texture class obtained by plotting the texture distribution in texture triangle, as well as mean and standard deviation of texture, bulk density (BD), apparent electrical conductivity (EC_a), last normalized difference vegetation (NDVI) data closest to the harvest, soil moisture deficit at harvest (SMD) calculated by subtracting the actual soil water content (SWC) from the SWC at field capacity (at pF = 2) divided by the sampling depth (30 cm). In addition, the yield and number of potatoes per hectare and the nitrate residue in the soil right after harvest are shown. The statistical significance was tested at a significance level of 10%. EMI, electromagnetic induction; NDVI, NDVI of last image; NO**3** res., nitrate residue at harvest.

[a]sL, sandy loam; lS, loamy sand, S, sand.

[b]$H = 1$, $p < .1$ for unpaired two-sample significance t test.

clearly belonged to a specific zone were selected; few plots were marginally between the zones (see Figures 8a–8c).

For each management zone of the homogeneously managed fields, Table 7 compares the soil attributes and yield information when using the clustering results based on either EMI or NDVI. The properties inside the zones for an unequal amount of trial plots were tested for a 10% significance level. The zonation based on EMI data obtained more statistically different soil attributes and crop or harvest properties than the clustering using NDVI data. Already the locations of the trial plots inside the different zones obtained by using EMI or NDVI data were remarkably different for the fields BP2017 and BP2019. Although the NDVI-based clustering was highly scattered due to the relatively dense green vegetation at the time of image acquisition, the management zones based on EMI data were clearly delineated. At the field KvE2018, the zones and thus the trial plots inside the zones used for testing were similar. Since the NDVI data acquisition was seasonally late (a few days before harvest), the crop patterns resembled the spatial soil distributions.

In the content-rich Table 7, we see that for the EMI-based zonation in both BP fields large differences were present in EC_a, whereas the differences in soil texture and bulk density were comparably small and large, respectively. However, a clear relation between EC_a and bulk density seems difficult given the observation of a positive correlation at both BP fields and a negative correlation at the field KvE2018. Considering harvest information, the zones were different in yield and potato counts. Note that the soil still contained relatively large amounts of nitrate residues. This agronomically shows that similar yield can be expected when using reduced and potentially zone-specific varying fertilization rates.

Summarizing, the EMI-based clustering delineates zones where the soil interacts and supplies the potatoes differently. The spatial soil patterns measured with EMI are time independent (considering time $\ll$ geochronological age) such that similar zonation is expected for measurements at any time in the year. Though De Benedetto et al. (2013) found that crops can be more sensitive to the management practices than to the intrinsic soil property, this study indicates that clear management zone delineation based on NDVI data depends on the data acquisition timing. In either way, we anticipate that the characterization of soil and intra-field variability strongly improve when fusing data of different proximal soil, as well as crop scanning sensors and harvest information. Such data fusion approaches help to obtain soil attribute maps with greater accuracy and potentially novel soil property models (Corwin & Scudiero, 2019), which consequently support farm-, field-, and zone-specific variable rate applications.

4 | CONCLUSIONS

We proposed a joint interpretation of ground-based EMI soil scanning data together with aerial drone-based crop data of NDVI and soil sampling data. The EMI data delineate field-scale management zones, where the nitrate residues and yield was different. Each management zone essentially showed specific agronomic soil quality. This knowledge enables the usage of zone-specific rates of fertilization and irrigation to cultivate the crops as successful while reducing nitrate leaching and saving irrigation water, which allows concluding that delineating the management zones using EMI is highly valuable to improve precision agriculture. A prerequisite to capture soil spatial variability is dense track spacing (e.g., parallel tracks $\geq$5–7 m).

The high-resolution soil information derived from large-scale EMI data showed detailed patterns in the soil attributes, which could not be derived from classical and coarsely resolved soil maps. Conclusively, the detailed information can better explain yield differences that may not be observed by high-resolution aerial crop data. Therefore, including the high-resolution soil data together with aerial crop data in agronomic modeling can improve the prediction of stress conditions and/or nutrient demands. The detailed soil maps can also inform pedotransfer functions, soil crop models, and machine learning techniques to improve soil, nutrient, and agro-chemical management in agricultural soils. This will help saving fertilization and irrigation amounts.

On the longer view, the findings in this paper can help changing the management practices toward sustainable intercropping and/or mixed cropping systems that select and adapt the crops according to the specific properties of each management zone. In a more future-directed way, the approach presented here may also help establish digital farming in terms of sustainable precision agriculture or even more out-of-the-box robotic-based permaculture. Such a shift needs to include the farmers in any debate, while exceedingly reducing the environmental impacts and damages and fulfilling the need to produce enough and highly nutritious food eventually at low costs.

FUNDING

ERA-NET Cofund WaterWorks2015 to support research on the sustainable management of water resources in agriculture, forestry, and freshwater aquaculture sectors. The WaterWorks2015 proposal responded to the Horizon 2020 (H2020) Societal Challenge 5 2015 Call topic Water-3 [2015].

ACKNOWLEDGMENTS

We thank Benjamin Mary for editor responsibilities, as well as Guiseppe Calamita and an anonymous reviewer for significantly improving the manuscript. We thank Joschka

Neumann and Ayhan Egmen, respectively working at the Institute of Engineering and Analytics, Technology (ZEA-1) and at the Institute for Bio-und Geosciences (IBG) of Forschungszentrum Jülich, for constructing and maintaining the EMI sleds. For help in the field, thank you to Gaël Dumont, Philipp Steinberger, Michael Iwanowitsch, Jessica Schmäck, Nicole Höring, Yenni Paloma Villa Acuna, Durra Saputera, Nassim Nassar, and Carlos Manuel Ocampo Ortiz. For discussing the data, thank you to Yves Brostaux and Hélène Soyeurt. We thank the Belgian farmers Koen van Eyck, Bert Peurteners, Patrick van Oeckel, and the Dutch farmer Jacob van den Borne for committing their fields and their interest in our studies.

CONFLICT OF INTEREST

The authors declare no conflict of interest.

ORCID

Christian von Hebel https://orcid.org/0000-0003-3521-1230
Klaas Pauly https://orcid.org/0000-0002-2183-1917
Pieter Janssens https://orcid.org/0000-0001-7571-396X
Isabelle Piccard https://orcid.org/0000-0002-1530-8468
Jan Vanderborght https://orcid.org/0000-0001-7381-3211
Jan van der Kruk https://orcid.org/0000-0003-2348-1436
Harry Vereecken https://orcid.org/0000-0002-8051-8517
Sarah Garré https://orcid.org/0000-0001-9025-5282

REFERENCES

Abdu, H., Robinson, D. A., Seyfried, M., & Jones, S. B. (2008). Geophysical imaging of watershed subsurface patterns and prediction of soil texture and water holding capacity. *Water Resources Research*, *44*. https://doi.org/10.1029/2008WR007043

Altdorff, D., von Hebel, C., Borchard, N., van der Kruk, J., Bogena, H. R., Vereecken, H., & Huisman, J. A. (2017). Potential of catchment-wide soil water content prediction using electromagnetic induction in a forest ecosystem. *Environmental Earth Sciences*, *76*. https://doi.org/10.1007/s12665-016-6361-3

Beamish, D. (2011). Low induction number, ground conductivity meters: A correction procedure in the absence of magnetic effects. *Journal of Applied Geophysics*, *75*, 244–253. https://doi.org/10.1016/j.jappgeo.2011.07.005

Bezdek, J. C. (1981). *Pattern recognition with fuzzy objective function algorithms*. New York: Springer Science + Business Media.

Binley, A., Hubbard, S. S., Huisman, J. A., Revil, A., Robinson, D. A., Singha, K., & Slater, L. D. (2015). The emergence of hydrogeophysics for improved understanding of subsurface processes over multiple scales. *Water Resources Research*, *51*, 3837–3866. https://doi.org/10.1002/2015WR017016

Boaga, J. (2017). The use of FDEM in hydrogeophysics: A review. *Journal of Applied Geophysics*, *139*, 36–46. https://doi.org/10.1016/j.jappgeo.2017.02.011

Brevik, E. C., Calzolari, C., Miller, B. A., Pereira, P., Kabala, C., Baumgarten, A., & Jordan, A. (2016). Soil mapping, classification, and pedologic modeling: History and future directions. *Geoderma*, *264*, 256–274. https://doi.org/10.1016/j.geoderma.2015.05.017

Brogi, C., Huisman, J. A., Pätzold, S., von Hebel, C., Weihermüller, L., Kaufmann, M. S., … Vereecken, H. (2019). Large-scale soil mapping using multi-configuration EMI and supervised image classification. *Geoderma*, *335*, 133–148. https://doi.org/10.1016/j.geoderma.2018.08.001

Calamita, G., Perrone, A., Brocca, L., Onorati, B., & Manfreda, S. (2015). Field test of a multi-frequency electromagnetic induction sensor for soil moisture monitoring in southern Italy test sites. *Journal of Hydrology*, *529*, 316–329. https://doi.org/10.1016/j.jhydrol.2015.07.023

Cassman, K. G. (1999). Ecological intensification of cereal production systems: Yield potential, soil quality, and precision agriculture. *Proceedings of the National Academy of Sciences*, *96*, 5952. https://doi.org/10.1073/pnas.96.11.5952

Castrignanò, A., Buttafuoco, G., Quarto, R., Parisi, D., Viscarra Rossel, R. A., Terribile, F., … Venezia, A. (2018). A geostatistical sensor data fusion approach for delineating homogeneous management zones in precision agriculture. *CATENA*, *167*, 293–304. https://doi.org/10.1016/j.catena.2018.05.011

Cavalcante Fraga, L. H., Schamper, C., Noël, C., Guérin, R., & Rejiba, F. (2019). Geometrical characterization of urban fill by integrating the multi-receiver electromagnetic induction method and electrical resistivity tomography: A case study in Poitiers, France. *European Journal of Soil Science*, *70*, 1012–1024. https://doi.org/10.1111/ejss.12806

Corwin, D. L., & Lesch, S. M. (2005). Apparent soil electrical conductivity measurements in agriculture. *Computers and Electronics in Agriculture*, *46*, 11–43. https://doi.org/10.1016/j.compag.2004.10.005

Corwin, D. L., & Plant, R. E. (2005). Applications of apparent soil electrical conductivity in precision agriculture. *Computers and Electronics in Agriculture*, *46*, 1–10. https://doi.org/10.1016/j.compag.2004.10.004

Corwin, D. L., & Scudiero, E. (2019). Review of soil salinity assessment for agriculture across multiple scales using proximal and/or remote sensors. *Advances in Agronomy*, *158*, 1–130. https://doi.org/10.1016/bs.agron.2019.07.001

De Benedetto, D., Castrignano, A., Diacono, M., Rinaldi, M., Ruggieri, S., & Tamborrino, R. (2013). Field partition by proximal and remote sensing data fusion. *Biosystems Engineering*, *114*, 372–383. https://doi.org/10.1016/j.biosystemseng.2012.12.001

Doolittle, J. A., & Brevik, E. C. (2014). The use of electromagnetic induction techniques in soils studies. *Geoderma*, *223–225*, 33–45. – https://doi.org/10.1016/j.geoderma.2014.01.027

Edwards, G. T. C., Hinge, J., Skou-Nielsen, N., Villa-Henriksen, A., Sørensen, C. A. G., & Green, O. (2017). Route planning evaluation of a prototype optimised infield route planner for neutral material flow agricultural operations. *Biosystems Engineering*, *153*, 149–157. https://doi.org/10.1016/j.biosystemseng.2016.10.007

Garré, S., Coteur, I., Wongleecharoen, C., Kongkaew, T., Diels, J., & Vanderborght, J. (2013). Noninvasive monitoring of soil water dynamics in mixed cropping systems: A case study in Ratchaburi Province, Thailand. *Vadose Zone Journal*, *12*. https://doi.org/10.2136/vzj2012.0129

GF Instruments, (2011). *CMD electromagnetic conductivity meter user manual V. 1.5*. Brno, Czech Republic: GF Instruments.

Gili, A., Álvarez, C., Bagnato, R., & Noellemeyer, E. (2017). Comparison of three methods for delineating management zones for site-specific crop management. *Computers and Electronics in Agriculture*, *139*, 213–223. https://doi.org/10.1016/j.compag.2017.05.022

Gonzalez-de-Santos, P., Ribeiro, A., Fernandez-Quintanilla, C., Lopez-Granados, F., Brandstoetter, M., Tomic, S., … Debilde, B. (2017). Fleets of robots for environmentally-safe pest control in agriculture. *Precision Agriculture*, *18*, 574–614. https://doi.org/10.1007/s11119-016-9476-3

Grunwald, S., Vasques, G. M., & Rivero, R. G. (2015). Fusion of soil and remote sensing data to model soil properties. *Advances in Agronomy*, *131*, 1–109. https://doi.org/10.1016/bs.agron.2014.12.004

Guillemoteau, J., Simon, F. X., Luck, E., & Tronicke, J. (2016). 1D sequential inversion of portable multi-configuration electromagnetic induction data. *Near Surface Geophysics*, *14*, 423–432. https://doi.org/10.3997/1873-0604.2016029

Hanssens, D., Delefortrie, S., Bobe, C., Hermans, T., & De Smedt, P. (2019). Improving the reliability of soil EC-mapping: Robust apparent electrical conductivity (rECa) estimation in ground-based frequency domain electromagnetics. *Geoderma*, *337*, 1155–1163. https://doi.org/10.1016/j.geoderma.2018.11.030

Heil, K., & Schmidhalter, U. (2012). Characterisation of soil texture variability using the apparent soil electrical conductivity at a highly variable site. *Computers & Geosciences*, *39*, 98–110. https://doi.org/10.1016/j.cageo.2011.06.017

Heil, K., & Schmidhalter, U. (2019). Theory and guidelines for the application of the geophysical sensor EM38. *Sensors*, *19*(19). https://doi.org/10.3390/s19194293

Huang, J., Koganti, T., Santos, F. A. M., & Triantafilis, J. (2017). Mapping soil salinity and a fresh-water intrusion in three-dimensions using a quasi-3d joint-inversion of DUALEM-421S and EM34 data. *Science of the Total Environment*, *577*, 395–404. https://doi.org/10.1016/j.scitotenv.2016.10.224

Huang, J., Scudiero, E., Choo, H., Corwin, D. L., & Triantafilis, J. (2016). Mapping soil moisture across an irrigated field using electromagnetic conductivity imaging. *Agricultural Water Management*, *163*, 285–294. https://doi.org/10.1016/j.agwat.2015.09.003

Hunkeler, P. A., Hendricks, S., Hoppmann, M., Paul, S., & Gerdes, R. (2015). Towards an estimation of sub-sea-ice platelet-layer volume with multi-frequency electromagnetic induction sounding. *Annals of Glaciology*, *56*, 137–146. https://doi.org/10.3189/2015AoG69A705

Jadoon, K. Z., Moghadas, D., Jadoon, A., Missimer, T. M., Al-Mashharawi, S. K., & McCabe, M. F. (2015). Estimation of soil salinity in a drip irrigation system by using joint inversion of multicoil electromagnetic induction measurements. *Water Resources Research*, *51*(5). https://doi.org/10.1002/2014WR016245

Janssens, P., Garré, S., Reynaert, S., Dumont, G., von Hebel, C., Piccard, I., … Boij, J. (2020). *Variable rate irrigation and nitrogen fertilization in potato; engage the spatial variation (POTENTIAL)*. Heverlee: Soil Service Belgium. Retrieved from http://hdl.handle.net/2268/246438

Kamilaris, A., & Prenafeta-Boldú, F. X. (2018). Deep learning in agriculture: A survey. *Computers and Electronics in Agriculture*, *147*, 70–90. https://doi.org/10.1016/j.compag.2018.02.016

Kaufman, L., & Rousseeuw, P. J. (1990). *Finding groups in data: An introduction to cluster analysis*. Hoboken, NJ: John Wiley & Sons.

Kaufmann, M. S., von Hebel, C., Weihermüller, L., Baumecker, M., Döring, T., Schweitzer, K., … van der Kruk, J. (2020). Effect of fertilizers and irrigation on multi-configuration electromagnetic induction measurements. *Soil Use and Management*, *36*, 104–116. https://doi.org/10.1111/sum.12530

Keller, G. V., & Frischknecht, F. C. (1966). *Electrical methods of geophysical prospecting. International Series of Monographs in Electromagnetic Waves*. Oxford, UK, and New York: Pergamon Press.

Lavoué, F., van der Kruk, J., Rings, J., Andre, F., Moghadas, D., Huisman, J. A., … Vereecken, H. (2010). Electromagnetic induction calibration using apparent electrical conductivity modelling based on electrical resistivity tomography. *Near Surface Geophysics*, *8*, 553–561. https://doi.org/10.3997/1873-0604.2010037

Maes, W. H., & Steppe, K. (2019). Perspectives for remote sensing with unmanned aerial vehicles in precision agriculture. *Trends in Plant Science*, *24*, 152–164. https://doi.org/10.1016/j.tplants.2018.11.007

Martinez, G., Vanderlinden, K., Ordóñez, R., & Muriel, J. L. (2009). Can apparent electrical conductivity improve the spatial characterization of soil organic carbon? *Vadose Zone Journal*, *8*, 586–593. https://doi.org/10.2136/vzj2008.0123

Martini, E., Werban, U., Zacharias, S., Pohle, M., Dietrich, P., & Wollschläger, U. (2016). Repeated electromagnetic induction measurements for mapping soil moisture at the field scale: Validation with data from a wireless soil moisture monitoring network. *Hydrology and Earth System Sciences*, *21*, 495–513. https://doi.org/10.5194/hess-21-495-2017

Mary, B., Peruzzo, L., Boaga, J., Cenni, N., Schmutz, M., Wu, Y. X., … Cassiani, G. (2020). Time-lapse monitoring of root water uptake using electrical resistivity tomography and mise-a-la-masse: A vineyard infiltration experiment. *Soil*, *6*, 95–114. https://doi.org/10.5194/soil-6-95-2020

McBratney, A. B., & de Gruijter, J. J. (1992). A continuum approach to soil classification by modified fuzzy *k*-means with extragrades. *Journal of Soil Science*, *43*, 159–175. https://doi.org/10.1111/j.1365-2389.1992.tb00127.x

McNeill, J. D. (1980). *Electromagnetic terrain conductivity measurement at low induction numbers*. Mississauga, ON, Canada: Geonics.

Mester, A., van der Kruk, J., Zimmermann, E., & Vereecken, H. (2011). Quantitative two-layer conductivity inversion of multi-configuration electromagnetic induction measurements. *Vadose Zone Journal*, *10*, 1319–1330. https://doi.org/10.2136/vzj2011.0035

Minsley, B. J., Kass, M. A., Hodges, G., & Smith, B. D. (2014). Multielevation calibration of frequency-domain electromagnetic data. *Geophysics*, *79*, E201–E216. https://doi.org/10.1190/geo2013-0320.1

Mulla, D. J. (2013). Twenty five years of remote sensing in precision agriculture: Key advances and remaining knowledge gaps. *Biosystems Engineering*, *114*, 358–371. https://doi.org/10.1016/j.biosystemseng.2012.08.009

Nawar, S., Corstanje, R., Halcro, G., Mulla, D., & Mouazen, A. M. (2017). Delineation of soil management zones for variable-rate fertilization: A review. *Advances in Agronomy*, *143*, 175–245. https://doi.org/10.1016/bs.agron.2017.01.003

Panda, S., Sahu, S., Jena, P., & Chattopadhyay, S. (2012). Comparing fuzzy-*c* means and *k*-means clustering techniques: A comprehensive study. In D. C. Wyld, J. Zizka, & D. Nagamalai (Eds.), *Advances in computer science, engineering & applications* (pp. 451–460). Berlin, Heidelberg: Springer. https://doi.org/10.1007/978-3-642-30157-5_45

Rascher, U., Alonso, L., Burkart, A., Cilia, C., Cogliati, S., Colombo, R., … Zemek, F. (2015). Sun-induced fluorescence: A new probe of

photosynthesis: First maps from the imaging spectrometer *HyPlant*. *Global Change Biology*, *21*, 4673–4684. https://doi.org/10.1111/gcb.13017

Robinet, J., von Hebel, C., Govers, G., van der Kruk, J., Minella, J. P. G., Schlesner, A., … Vanderborght, J. (2018). Spatial variability of soil water content and soil electrical conductivity across scales derived from electromagnetic induction and time domain reflectometry. *Geoderma*, *314*, 160–174. https://doi.org/10.1016/j.geoderma.2017.10.045

Robinson, D. A., Abdu, H., Lebron, I., & Jones, S. B. (2012). Imaging of hill-slope soil moisture wetting patterns in a semi-arid oak savanna catchment using time-lapse electromagnetic induction. *Journal of Hydrology*, *416*, 39–49. https://doi.org/10.1016/j.jhydrol.2011.11.034

Rousseeuw, P. J. (1987). Silhouettes: A graphical aid to the interpretation and validation of cluster analysis. *Journal of Computational and Applied Mathematics*, *20*, 53–65. https://doi.org/10.1016/0377-0427(87)90125-7

Saey, T., De Smedt, P., De Clercq, W., Meerschman, E., Islam, M. M., & Van Meirvenne, M. (2013). Identifying soil patterns at different spatial scales with a multi-receiver EMI sensor. *Soil Science Society of America Journal*, *77*, 382–390. https://doi.org/10.2136/sssaj2012.0276

Saifuzzaman, M., Adamchuk, V. I., Buelvas, R., Biswas, A., Prasher, S., Rabe, N., … Ji, W. (2019). Clustering tools for integration of satellite remote sensing imagery and proximal soil sensing data. *Remote Sensing*, *11*(9). https://doi.org/10.3390/rs11091036

Schröter, I., Paasche, H., Doktor, D., Xu, X., Dietrich, P., & Wollschläger, U. (2017). Estimating soil moisture patterns with remote sensing and terrain data at the small catchment scale. *Vadose Zone Journal 16*(10). https://doi.org/10.2136/vzj2017.01.0012

Stetco, A., Zeng, X.-J., & Keane, J. (2015). Fuzzy C-means++: Fuzzy C-means with effective seeding initialization. *Expert Systems with Applications*, *42*, 7541–7548. https://doi.org/10.1016/j.eswa.2015.05.014

Tan, X., Mester, A., von Hebel, C., Zimmermann, E., Vereecken, H., van Waasen, S., & van der Kruk, J. (2018). Simultaneous calibration and inversion algorithm for multi-configuration electromagnetic induction data acquired at multiple elevations. *Geophysics*, *84*. https://doi.org/10.1190/geo2018-0264.1

Van Ranst, E., & Sys, C. (2000). *Eenduidige legende voor de digitale bodemkaart van Vlaanderen (Schaal 1:20 000)*. Ghent, Belgium: Ghent University.

Virnodkar, S. S., Pachghare, V. K., Patil, V. C., & Jha, S. K. (2020). Remote sensing and machine learning for crop water stress determination in various crops: A critical review. *Precision Agriculture*, *21*, 1121–1155. https://doi.org/10.1007/s11119-020-09711-9

von Hebel, C., Matveeva, M., Verweij, E., Rademske, P., Kaufmann, M. S., Brogi, C., … van der Kruk, J. (2018). Understanding soil and plant interaction by combining ground-based quantitative electromagnetic induction and airborne hyperspectral data. *Geophysical Research Letters*, *45*, 7571–7579. https://doi.org/10.1029/2018GL078658

von Hebel, C., Rudolph, S., Mester, A., Huisman, J. A., Kumbhar, P., Vereecken, H., & van der Kruk, J. (2014). Three-dimensional imaging of subsurface structural patterns using quantitative large-scale multiconfiguration electromagnetic induction data. *Water Resources Research*, *50*, 2732–2748. https://doi.org/10.1002/2013WR014864

von Hebel, C., van der Kruk, J., Huisman, J. A., Mester, A., Altdorff, D., Endres, A. L., … Vereecken, H. (2019). Calibration, conversion, and quantitative multi-layer inversion of multi-coil rigid-boom electromagnetic induction data. *Sensors*, *19*(21). https://doi.org/10.3390/s19214753

Wang, H., Wellmann, F., Zhang, T., Schaaf, A., Kanig, R. M., Verweij, E., … van der Kruk, J. (2019). Pattern extraction of topsoil and subsoil heterogeneity and soil-crop interaction using unsupervised Bayesian machine learning: An application to satellite-derived NDVI time series and electromagnetic induction measurements. *Journal of Geophysical Research: Biogeosciences*, *124*, 1524–1544. https://doi.org/10.1029/2019JG005046

Ward, S. H., & Hohmann, G. (1988). Electromagnetic theory for geophysical applications. In M. N. Nabighian (Ed.), *Electromagnetic methods in applied geophysics* (pp. 130–311). Tulsa, OK: Society of Exploration Geophysicists.

Weigand, M., & Kemna, A. (2017). Multi-frequency electrical impedance tomography as a non-invasive tool to characterize and monitor crop root systems. *Biogeosciences*, *14*, 921–939. https://doi.org/10.5194/bg-14-921-2017

Werban, U., Kuka, K., & Merbach, I. (2009). Correlation of electrical resistivity, electrical conductivity and soil parameters at a long-term fertilization experiment. *Near Surface Geophysics*, *7*, 5–14. https://doi.org/10.3997/1873-0604.2008038

Whalley, W. R., Binley, A., Watts, C. W., Shanahan, P., Dodd, I. C., Ober, E. S., … Hawkesford, M. J. (2017). Methods to estimate changes in soil water for phenotyping root activity in the field. *Plant and Soil*, *415*, 407–422. https://doi.org/10.1007/s11104-016-3161-1

Zhu, Q., Lin, H., & Doolittle, J. (2010). Repeated electromagnetic induction surveys for determining subsurface hydrologic dynamics in an agricultural landscape. *Soil Science Society of America Journal*, *74*, 1750–1762. https://doi.org/10.2136/sssaj2010.0055

SUPPORTING INFORMATION

Additional supporting information may be found online in the Supporting Information section at the end of the article.

How to cite this article: von Hebel C, Reynaert S, Pauly K, et al. Toward high-resolution agronomic soil information and management zones delineated by ground-based electromagnetic induction and aerial drone data. *Vadose Zone J*. 2020;e20099. https://doi.org/10.1002/vzj2.20099